

LA-UR-04- 3844

Approved for public release;
distribution is unlimited

Title:

FEASIBILITY STUDY: USING BACKGROUND RADIATION FOR RADIOGRAPHY

Author(s):

Chris Morris

Submitted to:

DOE Office of Scientific and Technical Information (OSTI)

Los Alamos
NATIONAL LABORATORY

Los Alamos National Laboratory, an affirmative action/equal opportunity employer, is operated by the University of California for the U.S. Department of Energy under contract W-7405-ENG-36. By acceptance of this article, the publisher recognizes that the U.S. Government retains a nonexclusive, royalty-free license to publish or reproduce the published form of this contribution, or to allow others to do so, for U.S. Government purposes. Los Alamos National Laboratory requests that the publisher identify this article as work performed under the auspices of the U.S. Department of Energy. Los Alamos National Laboratory strongly supports academic freedom and a researcher's right to publish; as an institution, however, the Laboratory does not endorse the viewpoint of a publication or guarantee its technical correctness.

LOS ALAMOS NATIONAL LABORATORY



3 9338 00937 4207

Feasibility Study: Using Background Radiation for Radiography

Morris, Chris

Abstract

This is the final report of a Laboratory-Directed Research and Development (LDRD) project at the Los Alamos National Laboratory (LANL). We have investigated the feasibility of using cosmic muon radiography for homeland defense, and compared the process to x-radiography approaches. Models of realistic shipping containers for use in the Monte Carlo radiation codes MCNPX GEANT were constructed. These were used to compare existing x-ray and gamma ray techniques with muon radiography.

1. Background and Research Objectives

Strategies to prevent nuclear weapons or the components needed to build them from becoming available to terrorists are currently being formulated. Components include tightly controlling the world's supply of fissile materials, reducing or diluting the material that is suitable for building nuclear weapons, and surveillance at transportation choke points to interdict the illicit transport of fissionable materials. It is this last effort that this report deals with.

The essential component of any nuclear explosive device is the fissile core. This material is radioactive, emitting gamma rays, alpha particles, and neutrons. Both gamma radiation and neutron emission allow detection at a distance of meters. Detection schemes deployed to date have measured the gamma radiation or have used horizontal x-ray radiography to image the material. The gamma radiation, however, is easily shielded with a few centimeters of lead, tungsten, or other heavy metal. The currently deployed radiography has been shown to be ineffective. X-ray radiography with currently deployed system has failed to detect depleted uranium in shipments made by ABC news in an effort to test these systems.

In this report we present results of studies of a set of common problems of both x-radiography and muon-radiography using Monte Carlo techniques. The goal is to identify the strengths and weakness of each method and to contrast the differences. A problem suite developed for studying this threat is presented in appendix A. X-ray simulation results are given in appendix B and C, and muon radiography results are shown in appendix D.

A system which deploys gamma ray and possibly neutron detection forces the use of some shielding. The shielding increases the mass of any threat object. The least visible and lowest mass geometry is achieved with a compact spherical object and a compact spherical shield. This is reflected in the threat objects defined in the appendix. It is clear the radiation detectors should be a part of any deployed system.

2. Importance to LANL's Science and Technology Base and National R&D Needs

Homeland defense is becoming an important LANL mission. This feasibility study contributes to evaluating techniques for detecting hidden cargos of nuclear materials, one of the major homeland defense issues.

3. Scientific Approach and Accomplishments

X-rays

Conventional x-radiography takes advantage of the absorption of penetrating radiation. For x-ray radiography, the brightness of a pixel in the image is determined by the absorption or scattering of the incident beam:

$$N = N_0 e^{-\frac{L}{L_0}}, \quad (1)$$

where L is the path length (areal density) through an object, and L_0 is the mean-free path for scattering or absorption. In practice, equation 1 needs to be integrated over the energy distribution of x-rays making this analysis a bit more complicated. The precision of radiographic measurements is limited by Poisson counting statistics of the transmitted flux,

$$\frac{\Delta L}{L_0} = \frac{1}{\sqrt{N}}. \quad (2)$$

One can solve this for the optimum L_0 for radiographing a system of thickness L with a given N_0 . The result is $L_0 = L/2$.

An average shipping container has a mean density of 0.3 gm/cm^3 and a column density across its shorter dimensions of about 72 gm/cm^2 . Finding high-Z material which may be concealed within large masses of medium-Z material requires the use of photons of high energy and penetrating power in the opacity minimum (where opacity is $1/L_0$) around 5 MeV. The mean free path of x-rays is approximately independent of material and is about 25 gm/cm^2 . This energy is higher than most commercial systems in use.

Cargo is generally loaded in the containers with its long dimension horizontal. The areal densities presented to horizontal radiography for legitimate cargo can easily exceed anything that can be reasonably penetrated with x-radiography. This leads to one conclusion of this study, that vertical radiography is likely to be more effective than horizontal radiography for detecting threats hidden in cargo like that presented in appendix A. Current systems being deployed use horizontal radiography.

Low penetration and high contrast are expected from the threats studied. However our studies show that backgrounds due to scattering within the cargo, in the detectors and from the material behind and surrounding the detectors reduce this contrast to levels that make the threats much less obvious, even when using fan beams. The scatter background is very geometry dependent. Further, the area densities in legitimate cargoes can easily be large enough to obscure the desired signal.

It is suggested in appendix B that some of these problems can be solved by using two views, even at relatively narrow angles. This suggestion requires further development. The reduction in contrast due to scatter is still likely to be problematic if high-Z compact objects need to be discriminated from medium-Z compact.

In figure 1 the results from a GEANT a simulation of a portion of threat object 1 (20 kg of HEU) in the center of scene c, an array of two layers of 20cm radius half density steel spheres on 50 cm centers. This is a difficult cargo that may not be encountered with great frequency. The simulated radiograph was constructed by taking the \log_{10} of transmission for a set of scans covering a half of a cell and compositing these into are larger section for clarity. When the object is placed between rows of steel spheres it is visible as a small dense object, but the transmission is several orders of magnitude higher than is obtained with a pencil beam, because of scatter background.

This makes a determination of the objects opacity density difficult to determine even when its geometry is known. It will be difficult to identify threats in containers of lumped steel cargo.

Plots of transmission versus position on a line through the center of the uranium ball, when it is unobstructed and when it is behind one steel sphere are shown in Figure 2. The transmission through the uranium with a pencil beam was predicted to be 10^{-5} . Scatter from the container walls, the detectors, and the shielding behind the detectors reduces the contrast due to the uranium to $5.4 \cdot 10^{-3}$ when it is unobstructed and to 0.22 when it is behind the iron sphere.

Visualization of threat objects with x-radiography may be possible in lower z normal cargo, but scatter background will limit quantitative identification. In structured medium z cargo visualization is difficult. The range of this technique can be increased by using vertical radiography, with the source and detectors collimated to control scatter background, and by implementing two-view radiography so that the geometric ambiguities can be resolved. Further collimation with focused Buckey collimation or flying spot radiography may reduce scattering background.

Muon Radiography

An alternative is provided by charged-particle¹ radiography using cosmic-ray muons. When energetic charged particles travel through matter, the Coulomb force between the particles and the atomic nuclei in the medium leads to a large number of small deflections of the particle trajectories. The nature of the Coulomb interaction leads to a cross section for scattering that is not integrable, but, in aggregate, the multiple scattering of a particle can be treated analytically.² To a good approximation, the angular distribution that results when a particle of momentum p traverses from a length of material l is given by

$$\frac{dN}{d\Omega} = \frac{1}{2\pi\theta_0^2} e^{-\frac{\theta^2}{2\theta_0^2}}, \quad (3)$$

where θ_0 , the multiple scattering angle, is given by

$$\theta_0 = \frac{14.1}{p\beta} \sqrt{\frac{l}{X_0}}. \quad (4)$$

Here β is the velocity of the particle in units of the speed of light, and X_0 is a material-dependent constant that characterizes the length scale for Coulomb effects such as multiple scattering and pair production:

$$X_0 = \frac{716}{Z(Z+1)\ln(287/\sqrt{Z})}. \quad (5)$$

Here, Z is the atomic charge, and the units are in gm/cm^2 . Equation 3 can be used to determine the thickness of the object, in radiation lengths, if the angular deflection of a particle or the angular dispersion of a beam of particles that traverses an object can be measured. This observation has formed the basis for new kinds of radiography that are finding rather broad application at LANL, including proton radiography (pRad) at the Los Alamos Neutron Science Center (LANSCE), electron radiography, and, most recently, muon radiography. X_0 is a strong function of Z so that high- Z objects result in much more scattering than lower- Z background.

Charged particles also scatter from electrons in the medium. Because the electrons are light, charged-particle scattering generally leads to continuous energy loss rather than to angular deflections. This energy-loss mechanism provides a method for detecting the particles. In proton and electron radiography, images can be formed on scintillator screens with high efficiency. For cosmic-ray muon radiography, the energy deposited in a multiwire drift detector is used to measure the trajectory of individual cosmic rays.

Multiple scattering leads to a stochastic trajectory through the medium. This is one of the limitations of charged particle radiography. Position resolution is ultimately limited by the scale established by the product multiple scattering angle and object thickness, $\Delta x = k\theta_0 l$, where k is a case dependent constant of order unity.

In a 10-cm-thick layer, a 3-GeV muon (the average cosmic-ray energy) will scatter with a mean angle of 2.3 mrad in water ($X = 36 \text{ cm}$), 11 mrad in iron ($X = 1.76 \text{ cm}$), and 20 mrad in tungsten

($X = 0.56$ cm). If the muon-scattering angle in an object can be measured and if its momentum is known, then the path length, L , can be determined to a precision of

$$\frac{\Delta L}{L} = \sqrt{\frac{2}{N}}, \quad (6)$$

where N , the number of transmitted muons, is very nearly equal to the number of incident muons. Thus each transmitted muon provides information about the thickness of the object.

The potential advantages of muon radiography are the long range of the muons and hence the ability to penetrate most cargos; the quantitative nature of the radiography provides the potential for automatic recognition of threats; the random distribution of incident particles provides three dimension information and random sampling. The major disadvantage is the fixed low rate.

A rapid detection algorithm based on the number of highly scattering muons in a voxel (called “muon crossing” or MC algorithm) is able to provide a reliable detection and three-dimensional localization of high- Z objects in many simulated scenes (appendix D). The result of applying the muon crossing algorithm to one minute of cosmic ray counting for the case presented above is shown in figure 3.

Uranium is a sufficiently strong scatterer when compared with the steel balls that the threat is easily visualized in the complicated cargo. Because the scattering angles of the muons are so small (in fact it is the scattering that is used for the radiography) there is no scatter background, and no confusion about what is a threat. This enables the possibility of automatic detection. Further, this is all accomplished with no radiation above background.

Comparison

We have simulated the same scene for both x-ray and muon radiography. The object was a 20 kg sphere ($r = 6.33$ cm) of high enrichment uranium at center of container (2.4 m _ 2.4m _ 12 m). The container contains two planes of $r = 20$ cm half-density Fe spheres, each in a square array with 50 cm center-to-center spacing. The x-ray (figure 1) was constructed from a series of line

scans using a fan beam of x-rays, uniformly distributed in energy from 0 to 10 MeV. The muon radiograph (figure 3) was generated using the muon crossing algorithm (appendix D), with a one minute exposure.

Although the object can be visualized when it is between rows of steel balls, the x-ray contrast does not easily identify the object as a threat. If the object is placed in the shadow of a steel ball this problem becomes worse. Further background reduction, above that obtained with the simple fan beam we used here, is necessary for this to be a useful technique. In addition, additional views are required to discriminate long thin vertical objects from compact high density objects.

The threat object is easily discriminated from the steel spheres for this same scene using a one minute cosmic ray muon exposure. Although by using improved algorithms this time might be shortened some, the cosmic ray rate puts a fundamental limit on counting time. In one minute about 100 cosmic rays pass through the object. It is difficult to believe that meaningful reconstructions are possible with fewer than half this number of measurements.

Publications

1. N.B. Konstantin, G.E. Hogan, C. Morris, W.C. Friedhorsky, A. Saunders, L.J. Schultz, and M.E. Teasdale, "Radiographic imaging with cosmic ray muons," ,
Nature 422 , 277 (2003) , (2003).
2. Konstantin N. Borozdin, John J. Gomez, Gary E. Hogan, Christopher L. Morris,
William C. Friedhorsky, Alexander Saunders, Richard C. Schirato, Larry J. Schultz,
"Scattering Muon Radiography and Its Application to the Detection of High-Z
Materials," Nuclear Science Symposium, Medical Imaging Conference, Portland,
Oregon, October 19 – 25, 2003 , (2003).
3. Friedhorsky, W.C., Borozdin, K.N., Hogan, G.E., Morris, C., Saunders, A., Schultz,
L.J., Teasdale, M.,, "Detection of high-Z objects using multiple scattering of cosmic
ray muons," Review of Scientific Instruments 74, 4294-4297 (2003) , (2003).
4. L.J. Schultz, K.N. Borozdin, J.J. Gomez, G.E. Hogan, J.A. McGill, C. Morris, W.C.
Friedhorsky, A. Saunders, M.E. Teasdale, "Image reconstruction and material Z

discrimination via cosmic ray muon radiography," *Nuclear Instruments and Methods in Physics Research*, in press (2003 , (2004).

References

1. N.B. Konstantin, G.E. Hogan, C. Morris, W.C. Priedhorsky, A. Saunders, L.J. Schultz, and M.E. Teasdale, "Radiographic imaging with cosmic ray muons," *Nature* **422** , 277 (2003); Priedhorsky, W.C., Borozdin, K.N., Hogan, G.E., Morris, C., Saunders, A., Schultz, L.J., Teasdale, M., "Detection of high-Z objects using multiple scattering of cosmic ray muons," *Review of Scientific Instruments* **74**, 4294-4297 (2003); and L.J. Schultz, K.N. Borozdin, J.J. Gomez, G.E. Hogan, J.A. McGill, C. Morris, W.C. Priedhorsky, A. Saunders, M.E. Teasdale, "Image reconstruction and material Z discrimination via cosmic ray muon radiography," *Nuclear Instruments and Methods in Physics Research*, in press (2003).
2. B. Rossi, *High-Energy Particles* (Prentice-Hall, NJ, 1952), p. 66.

Figure Captions

- 1 A composite of x-ray fan beam scans showing the iron balls and the threat object. The logarithm of transmission is plotted as a grey scale in the image. This is only a small portion of the total image.
- 2 Profiles through the threat object. Red) for the case shown in figure 1 with the object between rows. Blue) with one iron ball below the object.
- 3 The same scene used for the x-ray analysis present above, but analyzed with a one minute cosmic ray exposure and with the ray crossing algorithm discussed in appendix D.
- 4 See text for description.
- 5 See text for description.
- 6 See text for description.
- 7 See text for description.
- 8 See text for description.
- 9 See text for description.
- 10 See text for description.

- 11 Simulated 10 MeV fan-beam X-ray projection through center of 20 kg U sphere of Test Case 1.
- 12 10 MeV average energy fan-beam X-ray projection through steel spheres of Test Case 1c.
The location for the projection is 20.3 cm (8 inches) from the center of the distribution.
- 13 Muon radiograph of a test object: steel C-clamp set on a plastic plate with steel support beams. Experimental data obtained with prototype experiment described in text. The image reconstructed with the PoCA algorithm. 30 1-cm slices in vertical direction are presented from upper left to lower right corner. The border of the slice corresponding to the medium plane is highlighted (the object was centered in vertical direction). The shape of the object is easy to recognize.
- 14 Detecting a high-Z object with the MC algorithm. Upper left panel is based on 1-minute simulation of empty container with 20-kg uranium sphere in the middle (“low” background case). Upper right panel shows the same container with the same sphere filled with 11 tons of uniformly distributed iron (“medium” background). In lower left panel there are 55 steel spheres, each of 130 kg weight, placed in the container (“high” background case) where the exposure is 3 minutes for this panel. Lower right panel represent the same “medium” background case as the panel above it, but instead of the small uranium sphere the object in the middle is a large iron sphere with the same number of radiation lengths as small uranium spheres. Red color in each panel is proportional to the $2N$, where N is a number of highly scattered muons in a voxel. Green color is proportional to the average scattering in the voxel, $\sigma(\theta)$, and blue is proportional to the product of N and $\sigma(\theta)$. The uranium sphere is clearly detectable in each case and is easily distinguishable from the large iron sphere.

Appendix A: Problem Suite for Container Radiography

G. Blanpied, K. Borozdin, G. Hogan, J. Katz, C. Morris and R. Schirato

The following threat objects were always taken to be at the center of the container:

1. 20 kg sphere ($r = 6.33$ cm, 20.6 radiation lengths) of uranium (90% ^{235}U , 10% ^{238}U) at center of container (2.4 m \times 2.4m \times 12 m). No external shield is assumed; an additional 5 mm of Pb would be sufficient to shield the soft gamma-rays of ^{235}U to $0.1 \text{ cm}^{-2} \text{ sec}^{-1}$ at 3.5 m; this is negligible, and sufficient shielding would probably be provided in any case by other materials. a. Container empty b. Container filled with Fe at $\rho = 0.3 \text{ g cm}^{-3}$ (20 metric tons) c. Container contains $r = 20$ cm half-density Fe spheres. There are two planes of these spheres, each in a square array with 50 cm center-to-center spacing, for a total of 240 spheres (32 metric tons, approximately the weight limit). The planes are centered 21 cm and 62 cm from the container floor (these distances are chosen to maintain clearances with the large solid iron sphere in series 4). The calculations include only one element of each plane, and these elements are centered on the z-axis, directly under the centers of the test objects.
2. 5 kg sphere ($r = 4.22$ cm, 11.9 radiation lengths) of δ -plutonium (94% ^{239}Pu , 6% ^{240}Pu at center of container. Such a sphere of Pu would be readily detectable by its gamma-emission, and in a realistic threat would have to be surrounded by at least 3 cm of Pb, which would give it radiographic properties similar to those of the larger U sphere of Problem 1, or by a larger shield of equivalent properties. Hence this problem (the calculation was performed without any shield) is probably an unrealistically difficult challenge for any detection method. Subcases a--c as for 1.
3. Lead pig (cylindrical, $r = 5$ cm, $h = 10$ cm, designed so that it presents a minimum of 3 cm of shielding for contents) with central cavity (cylindrical, $r = 2$ cm, $h = 4$ cm) filled with 800 gm of δ -Pu. This is designed to reduce the gamma-ray flux from ^{239}Pu decay to $0.04 \text{ cm}^{-2} \text{ sec}^{-1}$ at a distance of 3.5 m. If the plutonium contained 0.4% ^{241}Pu when fresh, and but which has all decayed ($t_{1/2} = 13$ years) to ^{241}Am the gamma-ray flux at 3.5 m would be $0.1/\text{cm}^2/\text{sec}$. 3 cm of Pb is 5.4 radiation lengths and 2 cm of Pu is 5.6 radiation lengths, for a total of 11.0 radiation lengths, giving this configuration muon scattering properties similar to those of the Pu sphere (2). This minimal pig would be sufficient to shield a significant quantity of Pu (although not in a shape which could be readily assembled into a nuclear explosive), but shielding a radiological weapon would require a much greater thickness of Pb because of the greater radiation intensity and (for some isotopes) the greater penetrating power of its gamma-rays. Hence this problem may be an unrealistically difficult challenge for any method. Subcases a--c as for 1.

4. 1690 kg sphere ($r = 37.3$ cm) of Fe, matching the number of radiation lengths in 1.
Subcases a--c as for 1.
5. 326 kg sphere ($r = 21.5$ cm) of Fe, matching the number of radiation lengths in 2.
Subcases a--c as for 1. Note that this case has approximately the same transmission as 1.
6. No threat object. This is a control run necessary only for subcase c, but is done for both normal and oblique incidence.

Matching of number of radiation lengths (1 vs. 4; 2 and 3 vs. 5) is for comparison to muon methods, for which the number of radiation lengths determines the distribution of scattering angles. Matching of absorption (1 vs. 5 in the Empty Container series) illustrates Z discrimination on the basis of the size of the attenuator.

Appendix B: Analysis of x-radiography

Jonathon Katz

A number of methods have been proposed to detect covert shipments of uranium or plutonium in shipping containers. One such method is photon radiography at energies of several MeV. The reason for using such high energies (higher than obtainable from radioisotope decay) is that material opacities decrease with energy until a broad minimum is reached, typically at energies of 5--10 MeV for medium-high Z materials (but depending on the material). The contents of an average shipping container have a mean density of 0.3 gm/cm^3 and a column density across its shorter dimensions of about 72 gm/cm^2 . Hence, to keep attenuation below 3 e-folds requires an opacity of less than $0.04 \text{ cm}^2/\text{gm}$. For such low opacity is found only for photon energies > 2 MeV, and similar results apply for lower Z elements¹ (because the opacity is dominated by Compton scattering). In fact, to find high-Z material which may be concealed within large masses of medium-Z material requires the use of photons of even greater energy and penetrating power, generally in the opacity minimum around 5 MeV.

Here we present results of Monte Carlo (MCNPX) calculations of photon propagation through hypothetical containers containing threatening quantities of high-Z material. Some of the

¹ Except for hydrogen, which is only a minor constituent by weight of cargoes.

examples were chosen only because they represent nominal threats, while others were chosen because they represent potential “false positive” detections for muon radiographic methods. These are, of course, also potential “false positive” detections for photon methods. A few “false positives” are tolerable, because a small number of containers may be opened and inspected manually, or by tomographic methods, but this is time-consuming and expensive and must be minimized. Recall that about ~7,000,000 standard shipping containers enter the U.S. each year, while the rate of genuine threats is likely to be $< 0.1/\text{yr}$. Threats include not only fissionable material but large quantities of radioactive material (“dirty bombs”) shielded in a massive lead “pig”.

The problem suite is detailed in appendix A. In the first series of problems the radiation source is a 10 MeV electron beam directed downward, directly above the test objects, into a 0.7 cm thick tungsten converter lying on top of the container. This geometry produces a two-fold geometric magnification of the absorption pattern of objects in the container's midplane when imaged by detectors near its floor. The tungsten layer is 2.0 radiation lengths thick. Only about 0.5 radiation length is required to stop the electrons; the remaining tungsten serves to filter the electromagnetic radiation, and is probably thicker than necessary. The electron energy of 10 MeV was chosen because compact linear accelerators of this energy are readily available, and because the resulting photons produce few photo-neutrons and activation products. Approximate calculations (MITRE/JSR 03-130) have shown that activation and subsequent radiation exposure (even if the cargo is food which will be ingested) are negligible. The use of higher electron energies would improve the sensitivity to high-Z materials, and is probably also acceptable, but was not calculated.

In a more realistic operational configuration the source (electron beam and tungsten converter) would be several meters above the container. The second series of problems places the radiation source 5.3 m above the top of the container. This would eliminate the need for side-to-side slewing of the beam to image the entire container, would reduce the geometric magnification, would flatten the illumination profile, and would permit imaging of the entire container (including material near its upper edges) by a detector array extending only about two feet outside the container's footprint. In this second series, a simple wedge collimator is used to produce a narrow fan beam from the broad bremsstrahlung radiation pattern (broadened because the electrons are scattered in the tungsten). This reduces the fill-in of heavily absorbed portions

of the radiographic image by scattered radiation. Elevating the radiation source also makes the unscattered beam more accurately vertical, so that simple collimators (lead or tungsten tubes) around the detectors could provide additional discrimination against scattered radiation and improve the sensitivity to high-Z materials over the results calculated here. Commercial linear accelerators provide orders of magnitude more flux than is required to scan containers moving under them at speeds of several m/sec, so that the loss of intensity to collimators, and by raising the source, acceptable.

In the calculations a lower energy cutoff on both electrons and photons of 100 keV was taken. This increased computational efficiency by eliminating a large number of low energy knock-on events. In practice, such low energy photons are undesirable for both imaging and radiological safety reasons because they scatter roughly isotropically (and efficiently in low-Z materials). Thin lead sheets in the ground and above the detectors (not included in the calculations) would discriminate effectively against this scattered radiation, and essentially eliminate earthshine (scattering of radiation from the ground back to the environment). Imaging would take place in lead-lined enclosures, with flap doors, analogous to those used in airport luggage screening.

Downward illumination, as assumed here, is desirable for several reasons:

1. It minimizes the use of scarce ground space, particularly if the radiation source is elevated several meters above the top of the container.
2. Downward propagating gamma-rays will be absorbed by the earth, minimizing the required shielding. This is particularly important for the most energetic gamma-rays, which are hardest to shield, but which scatter almost entirely in the forward direction.
3. It permits several meters standoff between the radiation source and the imaged container. Long slender objects of medium-Z material (axles, shafts, {\it etc.}) are unlikely to be packed with their long axes vertical, and hence will not be false positives for compact objects of high-Z material.

Results

Five potential threats were considered, each concealed within three possible container loads, as detailed in the appendix A. In the first series of calculations (Figures 4-7) the radiation source is uncollimated and is on the upper surface of the container. Figure 4 shows the results obtained if the container is empty (except for the threat); the container itself, typically consisting of steel

walls 3 mm thick and reinforcing beams, was ignored. The Figures show the calculated energy deposition (per source electron) at point detectors 5 cm below the bottom of the container; because the accelerators are pulsed, there is no attempt to resolve individual photons. The detector locations are measured from a point directly under the vertical axis running from the electron source through the axis of the threat.

The high-Z threats are characterized by their compact size and two to three orders of magnitude of attenuation compared to the unattenuated flux (which is a slowly declining function of location, reflecting the finite width of the photon beam emerging from the tungsten converter). Note the factor of two geometric magnification resulting from placing the source on the top surface of the container.

The large iron spheres were chosen so that they have the same number of radiation lengths as the uranium and plutonium threats. The reason for this is that the muon scattering angles are determined entirely by the number of radiation lengths. Hence these iron spheres represent potential false positives for muon radiography, which can be distinguished from genuine threats by their greater size upon track reconstruction. In photon radiography the iron spheres are also distinguishable from the high-Z threats by their greater size. Even when their absorptions are well matched (as for the 6.33 cm U sphere and the 21.5 cm Fe sphere; that this is an accidental coincidence, for this Fe sphere was chosen to match the number of radiation lengths of the 4.22 cm Pu sphere) the genuine threat and potential false positive are readily distinguished by their geometrical extent.

A recurrent question in radiography is how to distinguish a massive medium-Z object (a large casting, electric motor, ingot or rod stock, *etc.*) from a compact, equally attenuating, high-Z threat. In general they may be distinguished on that basis of their extent in the transverse dimension. The chief exception, in the case of photon radiography, would be a long slender object viewed end-on. The use of vertical illumination largely eliminates this possibility because such objects are rarely shipped in a vertical orientation; if it remains a concern it may be addressed by a second radiograph taken with oblique illumination.

In Figure 5 the calculations are repeated with the container (outside the threat object) filled with iron to a mean density of 0.3 gm/cm^3 , producing a container with a total mass of about 20 tons.

The most striking result is that the darkness of the shadow of the threat objects is greatly reduced by radiation scattered (or reradiated by Compton electrons) within the container fill. Despite this, a contrast of roughly three-fold is still found at the edge of the shadow of the threat objects. Their small size remains apparent, especially in comparison to the very broad shadows of the false positives. Just as for the empty container, a medium-Z false positive whose attenuation is the same as that of a high-Z object would be much larger, except in the rare case of a slender object shipped with its long axis vertical (this is not explicitly shown).

This series of calculations was chosen because there has been some discussion of the possibility that that matter filling the container, but at some distance from threat object, might reduce the ability of muon radiography to distinguish a very compact high-Z threat object from a much larger medium-Z potential false positive. The calculations reported here cannot, of course, address that question; they were performed to show how well (or poorly) photon radiography deals with the same problem.

In Figure 6 the calculations were repeated without a uniform fill, but adding two Fe spheres of half solid density and 20 cm radius directly under the threat objects, with the spheres' centers 21 cm and 82 cm above the container floor. This was chosen to represent a container with 32 tons of these spheres, distributed in two layers of 120 spheres each; each sphere represents a casting (automotive engine block), electric motor or similar object of mass 132 kg.

In this calculation the Monte Carlo statistics in the most heavily shadowed regions were quite poor, accounting for the irregular nature of the energy fluxes there (elsewhere in this Figure, and everywhere in Figures 4 and 5, the estimated relative errors were generally less than 0.05, and at a few points only slightly in excess of that).

In Figure 6 the calculations containing compact high-Z threat objects chiefly show the shadows of the lower density balls. In fact, the shoulder on the curves between 22.5 cm and 25 cm, though poorly resolved, appears to distinguish the shadows of the two balls (which have different geometric magnifications). The shadows of the compact high-Z threat objects appear to be largely washed out by radiation scattered by the medium-Z balls, although there is some evidence for the edge of the 6.33 cm U sphere around 12.5--15 cm (where it would be expected, given the geometrical magnification). Comparison of a control problem (no threat target) to the

calculation with the U sphere supports the suggestion that some evidence for the sphere is present. These calculations need to be repeated with improved variance reduction to determine if it is possible to determine reliably the presence of these threat objects under these conditions.

It should not be a surprise that the attenuation of 314 gm/cm^2 of iron (the column density through the diameters of the two balls) makes it difficult or impossible to detect compact threat objects. Even were the calculation without statistical fluctuations and the calculated images sharp, detecting them in the real world would require a dynamic range of 10^4 . This is probably unrealistic. There are two possible solutions to this problem: 1) The use of a higher energy electron accelerator, making more energetic gamma-rays, for which the ratio of high-Z to medium-Z opacities is greater. 2) The use of a second, oblique exposure. A slew of 12° is sufficient (in the assumed geometry) for a ray through the origin of the threat object to miss the upper ball, and 20° is sufficient for such a ray to miss both balls. A mechanical slew is possible, but it would probably be easier simply to take advantage of the finite width of the photon beam (using a second detector array displaced along the container's path by a suitable distance).

Figure 7 shows the results from calculations of a second, oblique, angle of illumination under these conditions (the deep shadows of the balls in Figure 8 are a tell-tale that their absorption could be concealing more compact objects, and could be an operational indicator of the need for an oblique second radiograph). The eight balls near the line of sight from the source are included. Comparison to the control (no threat object) curve in Figure 7 shows that oblique illumination (the angle used makes the line of sight skirt the lower of the two balls directly below the threat object) will reveal the presence of compact threat objects, and show their characteristic small sizes. Attenuation by a neighboring ball appears in the rightmost bin of the curves. The large iron spheres introduced as potential false positives for muon radiography are not included in Figure 7 because they would be readily recognized by the depth and width of their shadows.

Figures 8-10 repeat most of the preceding calculations with the radiation source raised to 5.3 m above the top of the container, and with a wedge collimator of opening angle $11'$ immediately below the tungsten converter slab. This narrow opening angle was chosen to illuminate a swath 2.5 cm wide, transverse to the long container axis, on the detector plane. Comparison of Figure 4 to Figure 8, and especially of Figure 5 to Figure 9 and Figure 6 to Figure 10 shows how collimating the illuminating beam drastically increases the contrast (by about two orders of

magnitude for the latter two comparisons). Such a fan beam is naturally matched to a (transverse) one-dimensional detector array.

Of course, no amount of contrast can solve the problem, evident in Figures 6 and 10, of excessive absorption by container contents. Detector systems have finite dynamic range, limited both by detector characteristics and by counting statistics when the attenuation is high. As illustrated in Figure 6, the solution to this problem is to image the container obliquely as well as vertically. A dense compact object will produce deep absorption for all directions of illumination, while a less dense long and slender object will only produce deep absorption along its axis. In the case of the iron balls of Figures 6, 7 and 10 directions through the diameters of two balls are equivalent to directions along the major axis of a long slender object.

It would be straightforward (although the calculation has not yet been done) to modify the collimator to produce a second fan beam of illumination, and to provide an additional line of detectors. In practice, it might be useful to arrange to move the direction of one of the beams (and appropriately displace the corresponding detectors) frequently (daily or weekly) so that an adversary could not anticipate the direction of illumination. Such measures may not actually be necessary; the operational response to a suspect container would be further investigation, perhaps by manual unloading and inspection. If the rate of false positives produced by a single fan beam is low enough, two-beam radiography would not be necessary.

Appendix C: GEANT x-radiography simulations

G. Blanpied and R. Schirato

For purposes of comparison between muon radiography and x-ray imaging, a simplified line-scan x-ray system was simulated using the GEANT 3 Monte Carlo code. The parameters of the system were selected to be representative of a class of high energy x-ray line scanners and to elucidate certain features of the technology, while being simple enough to model cost effectively. A fan-beam collimated source of 10 MeV photons was located at 5.0 m above the detector plane. The angular distribution of the photons followed a cosine relationship until truncated at the edge

of the detector array. Each pixel detector was modeled by a piece of NaI scintillator 1.27 cm transverse to the mechanical scan direction, and 2.54 cm both along the scan direction and in thickness. The line array was composed of 400 of such detector elements, with the beam directed downward at the center of the array. The width of the fan beam was selected to be 5.08 cm to over-fill the detector array.

Our 2.4 m x 2.4 m cross section container with 1.0 mm thick steel walls was placed directly below the beam and 10 cm above the detector array. (With such a geometry, the upper corners of the container are not imaged. Since our test cases have the objects of interest at the center, this was deemed acceptable for the purposes of this study.) Images would then be generated by our simulated system by translating the container and enclosed test case objects relative to the fixed source and detector, or vice versa. Ten million photons were tracked for each line projection. In order to simulate current-mode operation appropriate for a pulsed electron accelerator source, total energy deposited in each detector element was tallied.

Radiation scattered from other parts of the object and from shielding behind the detector is an important limiting factor for the contrast achievable by a high energy x-ray imaging system. In fact, that is why fan-beam geometry is often chosen for this type of application, as was modeled here. One inch of aluminum and six inches of concrete were placed behind the detector array to simulate the sensor electronics, supports, and shielding/structure which would back-scatter some of the incident photons.

A simulation with a pencil beam has been used to determine the ideal attenuation factor for the 20 kg Uranium sphere of Test Case 1. This yields an attenuation of 1×10^{-5} through the center of the sphere. At first glance, such a large relative attenuation factor could be considered as a good way to detect such high density, high Z SNM. Issues of electronic dynamic range and incident photon statistics aside, scattered radiation places a limit on contrast achievable in any realistic imaging system. Moreover, the amount of scatter which “undercuts” the projection of the SNM is dependent upon the location and mass of the rest of the cargo, and on the distance from the SNM to the detector plane. Figure 11 shows an x-ray line profile for the 20 kg Uranium sphere placed at the center of the container calculated as described above. Energy deposited in each detector pixel is ratioed to that without a sample, and shown on a logarithmic scale. Notice that

the attenuation at the center of the sphere is only $\sim 5 \times 10^{-3}$. The lateral size of the projected image also depends upon the height of the object.

Figure 12 shows a representative line profile through some of the $r = 20$ cm, half density iron balls of Test Case 1c. In particular, this profile is for a position of 20.3 (8 inches) from the center of the distribution of the objects. One can see that the attenuation reaches a significantly higher ratio than that for the U sphere, and has a complex shape. High probability detection of the U sphere in such a cluttered background would be difficult, especially if the obscuring objects are somewhat randomized.

Appendix D: Scattering Muon Radiography and Its Application to the Detection of High-Z Materials

Konstantin N. Borozdin, John J. Gomez, Gary E. Hogan, Christopher L. Morris, William C. Priedhorsky, Alexander Saunders, Richard C. Schirato, Larry J. Schultz

Abstract-- Scattering muon radiography is a novel technique of 3-d imaging for dense high-Z objects. High-energy cosmic ray muons are deflected in matter in the process of multiple Coulomb scattering. Measuring the deflection angles we are able to reconstruct the configuration of high-Z material in the object. We discuss how the technique can be used for the detection of compact high-Z objects in a large volume of ordinary material. We present results of our experiments and simulations and discuss image reconstruction issues relevant to scattering muon radiography. The ability of the technique to detect 20 kg of uranium hidden inside more than 10 tons of iron and in less than a minute of exposure is demonstrated.

INTRODUCTION

NUCLEAR materials contraband is a serious and actual threat for the United States as well as for many other nations. Detection of such contraband is a challenge in view of the huge volume of border traffic. An ideal detection method should be safe, fast, effective and economical. The total time to inspect a sea container, commercial truck or passenger car for the presence of illicit nuclear material should be about one minute. An effective method should be able to detect a

small amount of nuclear material hidden in normal cargo with very low rate of false detection. Safety requirements complicate the procedure making it slower and more expensive.

Existing methods for nuclear contraband detection are based on the detection of radioactivity from nuclear materials or on their high stopping power to a penetrating beam of the X-rays or gamma-rays. Unfortunately, none of these methods is free from serious flaws. Radiation from nuclear materials can be relatively easily attenuated by a small amount of shielding. X-ray and gamma-ray screening expose a test object to an artificial dose of radiation, which prolongs and complicates the procedure, especially in case of passenger cars and buses (these vehicles typically are not inspected at all). X-rays suffer from insufficient penetrating ability, so that they may be stopped not only by uranium or plutonium, but also by a typical metal such as steel. X-ray and gamma-ray scanners provide two-dimensional gray-scale images and suffer from clutter. Additionally, the detection of the object of interest in the image is up to the human inspector, which further reduces the efficiency of the method. There were several media reports about successful smuggling of nuclear materials in a cargo screened by X-rays. Active interrogation methods combine both probing of the object with artificial radiation and detection of the response and also suffer from safety concerns and low efficiency.

Recently, we proposed an alternative method for nuclear contraband detection [1]. The Earth is constantly bombarded by high-energy cosmic rays. Primary cosmic rays interact with the atmosphere and produce secondary cosmic showers of high-energy particles. At low altitudes below 5 km most cosmic rays are positively and negatively charged muons, with an average flux of 10,000 particles per square meter per minute [2]. The average cosmic ray muon bears high energy (2-3 GeV) and is highly penetrating. This makes cosmic ray muon flux an ideal probe for large dense objects. Absorption of cosmic ray muons has been used for many years to probe very large objects – Egyptian pyramids, mountains etc. [3]-[5]. To make the method sensitive to small volumes of high-Z materials we propose to use multiple scattering of the muons in material [6,7].

Concept and Apparatus of Muon Scattering Radiography

Because of their high energy few muons stop in ordinary cargo in passenger cars or trucks. For effective muon radiography we need to use the information from multiple Coulomb scattering. Each muon moving through any material, from air to high-density nuclear materials, undergoes multiple small deflections due to its electromagnetic interaction with nuclei and electrons (muons are leptons, so electromagnetic and much weaker gravitational interactions are their only ways to interact with material). The many small deflections add up to yield an angular deviation of the

muon from its initial trajectory. The distribution of those deflections is roughly (to the accuracy of a few percent) Gaussian, with the width inversely proportional to the particle momentum and proportional to the thickness of the scattering medium measured in radiation lengths [2]:

$$\sigma_\theta \propto \frac{1}{p} \sqrt{\frac{L}{X}}, \text{ where } p \text{ is the muon momentum, } L \text{ is the depth of the material, and } X \text{ is the radiation}$$

length of the material. Radiation length is in turn a function of atomic mass A and atomic

$$\text{number } Z \text{ of the scattering material [8]: } X = \frac{716.4A}{Z(Z+1)\ln(287/\sqrt{Z})} \text{ (in g/cm}^2\text{). } A/Z \text{ is close to 2 for}$$

most of ordinary matter; as a result the width of muon scattering for an object of given thickness is roughly proportional to the square root of the product of the material density ρ by the material atomic number Z : $\sigma_\theta \propto \sqrt{\rho Z}$. Nuclear materials such as uranium and plutonium are both denser and have higher atomic numbers than ordinary plastic, concrete or steel. Measuring multiple scattering of cosmic ray muons hence allows us to detect nuclear materials in ordinary cargo.

To measure the scattering we need to measure a trajectory of each muon before and after interaction. The trajectory in the absence of any significant scattering is a straight line; it is described by two consecutive measurements of muon coordinates x and y in two planes of known vertical separation (z coordinate). We need four detector planes, two above and two below the object. Horizontal planes of detectors maximize the detection of vertical muons. Cosmic ray muons have a broad angular distribution, so covering larger solid angle increases the number of detected muons and improves sensitivity of the measurement for given exposure. Cost of the apparatus, however, increases roughly proportional to detector area. We propose to use four horizontal detector planes as a simple and cost-effective design. Large area muon detectors have been used in high-energy experiments for decades. High efficiency of muon detection in each plane is very important, because an event will be lost if not detected in each and every plane. Uncertainty of the scattering width measurement is dominated by the statistics of muons in a voxel, and knowledge of their momentum. Angular resolution of the system should be reasonably good to provide small contribution to the total uncertainty. Sub-millimeter spatial resolution of the detectors is sufficient for practical geometries.

The system is able to work without any measurements of the muon momenta, but its performance improves significantly when this knowledge can be obtained even approximately. Inexpensive energy measurement may be acquired from the additional positional sensitive detectors to measure the scattering of muons after some target of known thickness and radiation length (for example, steel or concrete slabs of known thickness). We showed that two additional detector planes placed below the plates of known thickness and material are able to provide an

estimate of the muon momenta with an accuracy of $\Delta p / p \approx 0.5$ [7]. Alternatively, muon momenta may be roughly estimated from the amplitude of a signal in proportional gas detectors or scintillators.

A full-scale system for the inspection of commercial truck would have a sensitive volume between detectors at least $8 \times 4.5 \times 4.5 \text{ m}^3$. It will use 4 to 6 horizontal detector planes each of $4.5 \times 8 \text{ m}^2$ and separated by 1 meter in vertical direction. Two or four detector planes will be likely put underground, with the remaining two planes at heights of 4.5 m and 5.5 m above. This is the geometry assumed in our simulations of full-scale system discussed below.

For experimental proof-of-principle we constructed a much smaller version with four $60 \times 60 \text{ cm}^2$ detectors separated by 25 cm along the z coordinate. The detectors were position sensitive delay line readout drift chambers [8]. Two plastic scintillators in coincidence with the outermost drift chambers provided a timing trigger required by the delay line detectors. Signals from the detectors were amplified and discriminated in standard NIM electronics, were digitized in FERA ADCs, and read into a computer using a PC based data acquisition system, PCDAQ [9]. The detectors measured position to a precision of about 400 mm full width at half maximum (FWHM), and angles to about 2 mrad FWHM. For this initial prototype no momentum measuring planes were implemented.

Image Reconstruction

With our experimental prototype we performed muon radiography with a set of test objects. It is important to note that the experimental apparatus does not produce an image immediately. Experimental data for each muon are four measurements of x and y muon coordinates in planes of known height z. Our goal is to reconstruct the object from these data. Parameter of interest is a radiation length of the material at each point of space or in every voxel of a three-dimensional image. We cannot reconstruct a path of each muon through the material, as the path is a result of a random walk caused by multiple independent interactions of the muon with matter. Our data allow us only to approximate the result of multiple scattering as a single scattering event. In fact, outgoing trajectory of the scattered muon does not need to cross its incident trajectory in three-dimensional space. We may use, however, a point of closest approach for these two tracks as a designated point of the scattering. Each muon is assigned to a voxel of three-dimensional image, which contains the point of closest approach for this muon. Average of squared measured scattering angles gives us an estimate for the material radiation length. We may now create a

three-dimensional image with the signal in each voxel inversely proportional to measured radiation length. Accuracy of the measurement is inversely proportional to the square root of the number of muons attributed to the voxel, when we know the muon momentum. For a hundred muons we would measure the radiation length of the material in a voxel with the uncertainty of 10%. In practical situations this accuracy cannot be achieved because of uncertainty of our knowledge of muon momenta. The method of image reconstruction described above is called the PoCA (point of closest approach) algorithm [7]. Applying the PoCA algorithm to the experimental data we were able to reconstruct test objects in three-dimensions as illustrated in Fig.13.

The PoCA algorithm works well when a single-scattering approximation is valid, i.e. in the absence of a significant amount of distributed scattering material. Unfortunately, in practical applications a distributed scatterer often cannot be excluded. Imaging, with the PoCA method, of a high-Z object located inside a train car filled with a coal or in a shipment of aluminum fence rolls is like a photograph of a fish in muddy water. Point of closest approach in these situations may be significantly shifted away from the object of interest.

Even though single-scattering approximation may not work in some cases, the angles of muon deflection are still so small that we know quite accurately what voxel each muon intersects. The broad angular distribution of the muons allows us to find the voxels with larger number of highly scattered muons. These are the voxels where compact high-Z objects may be located.

It appears that the detection algorithm based on the number of highly scattering muons in a voxel (called “muon crossing” or MC algorithm) is able to provide a reliable detection and three-dimensional localization of high-Z objects in many simulated scenes. Fig.14 shows several examples.

We simulated a full-scale muon radiography system described in the previous section. Data from our simulations were verified by comparison with the experimental prototype data for small objects and appeared to be in an excellent agreement [1]. For Fig.14 we simulated a $6 \times 2.4 \times 2.4$ m³ cargo container with 3 mm steel walls. In different simulation scenes the container was either empty, filled with 11 tons of uniformly distributed iron, or filled with 130-kg iron spheres to the load limit. These represent “low”, “medium” or “high” level of scattering background respectively. A uranium sphere of 6.3 cm radius and 20 kg of weight was simulated in the middle of the container. In each case voxels at the sphere position had more highly scattered muons than other voxels in the volume. In the last panel of Fig.14 we repeated the scene with “medium”

background, but instead of the small uranium sphere we used a large (1690 kg) sphere of solid iron matching the number of radiation lengths in uranium sphere. This object is clearly detectable in the image as a strong scatterer, but its size allows easy distinction from a compact uranium sphere.

To make the images shown in Fig.14 we selected 1,000 most strongly deflected muons out of about 100,000 muons simulated for 1 minute of exposure in full-scale system. This version of the MC algorithm does not produce a detailed picture of an inspected object. However, for contraband detection we do not care about shape of the objects, our concern is simply whether illicit high-Z material is present or not. To estimate how well the MC algorithm may answer this question we performed a hundred of the 1-minute simulations of the uranium sphere embedded in uniformly distributed iron (one such simulation is presented in Fig.14, upper right panel). We also made a hundred 1-minute simulations of the background scene (a container filled with uniformly distributed iron but without any high-Z objects). Our detection algorithm was very simple in this case: we considered an image “clean” if the maximum number of highly scattered muons in a $10 \times 10 \times 10 \text{ cm}^3$ voxel was 11 or below; otherwise a high-Z object was assumed to be detected. In the 200 simulated experiments we detected the presence of uranium sphere in 100% of the cases with no false positives. Fig.15 shows a distribution of the maximum number of highly scattered muons in a voxel for scenes with and without a high-Z object.

This simple thresholding method can be used in this case for automatic detection of the high-Z material. More sophisticated detection algorithms will be applied to ensure reliable detection of high-Z objects in a variety of different backgrounds.

Conclusions

We have proposed a new method for nuclear material contraband detection based on cosmic ray muon radiography [1], [6], [7]. The method is safe, because it does not include the generation of any artificial radiation, but uses naturally produced high-energy muons. Results obtained with our prototype experiment and from simulations demonstrate the feasibility of the method for the detection of high-Z materials hidden inside different types of ordinary cargo. Detector technology for muon detection is mature and enables cost-effective design for a muon radiography apparatus. Image reconstruction is not trivial and may be done in various ways. We discuss the PoCA algorithm developed for image reconstruction and the MC (muon crossing) algorithm for the detection of high-Z material. Our simulations of a full-scale muon radiography

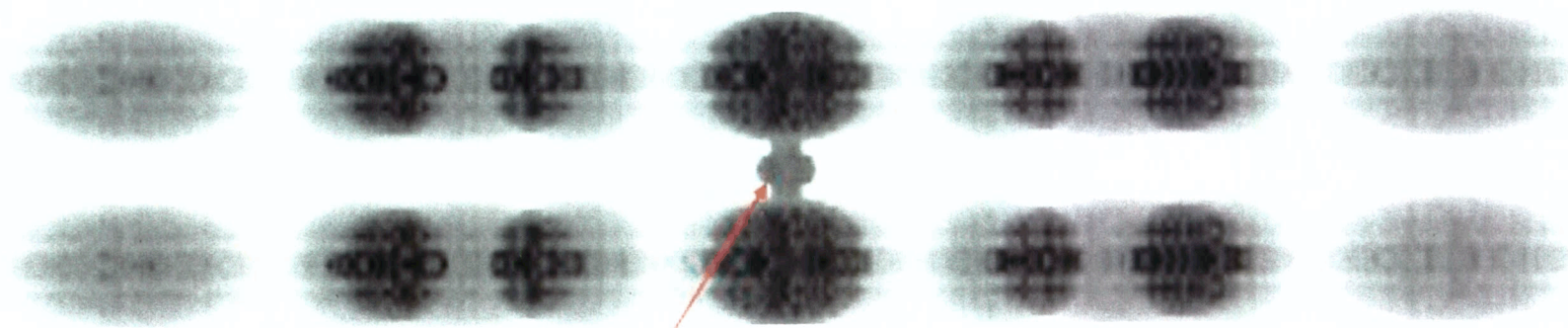
system suggest high efficiency of detection in 1 minute of exposure with a low number of false positives for a 20 kg of uranium hidden inside 11 tons of uniformly distributed iron.

Acknowledgments

We would like to thank Gary Blanpied for the muon generator, which became a part of our simulation software and Jonathan Katz for his help in the defining of simulation scenes.

References

1. Konstantin N. Borozdin, Gary E. Hogan, Christopher Morris, William C. Priedhorsky, Alexander Saunders, Larry J. Schultz, Margaret E. Teasdale, "Radiographic Imaging with Cosmic Ray Muons", *Nature*, 422, 277, 2003
2. Hagiwara, K., et al., Particle Data Group, Review of Particle Physics, *Phys Rev D* 66, 1, 2002
3. George, E. P., "Cosmic Rays Measure Overburden of Tunnel," *Commonwealth Engineer*, July 1, 1955, pp 455-457 (1955).
4. Alvarez, L.W., et al., "Search for Hidden Chambers in the Pyramids," *Science* 167, pp 832-839, 1970
5. Minato, S., "Feasibility of Cosmic-Ray Radiography: A Case Study of a Temple Gate as a Testpiece," *Materials Evaluation* 46, pp 1468-1470, 1988
6. Priedhorsky, W.C., Borozdin, K.N., Hogan, G.E., Morris, C., Saunders, A., Schultz, L.J., Teasdale, M. "Detection of High-Z Objects using Multiple Scattering of Cosmic Ray Muons," *Review of Scientific Instruments*, 74(10), pp 4294-7, 2003
7. Schultz, L.J., Borozdin, K.N., Gomez, J.J., Hogan, G.E., McGill, J.A., Morris, C.L., Priedhorsky, W.C., Saunders, A., and Teasdale, M.E., "Image Reconstruction and Material Z Discrimination via Cosmic Ray Muon Radiography", *Nucl. Instrum. Meth.*, in press, 2003
8. Atencio, L. G., Amann, J. F., Boudrie, R. L., and Morris, C. L. Delay-Line Readout Drift Chambers. *Nuclear Instruments & Methods In Physics Research* 187, 381, 1981
9. Hogan, G. E., "PC DAQ : a personal computer based data acquisition system," Los Alamos National Laboratory LA-UR-98-4531, 1998, <http://lib-www.lanl.gov/cgi-bin/getfile?00418755.pdf>.



Uranium ball

FIGURE 1

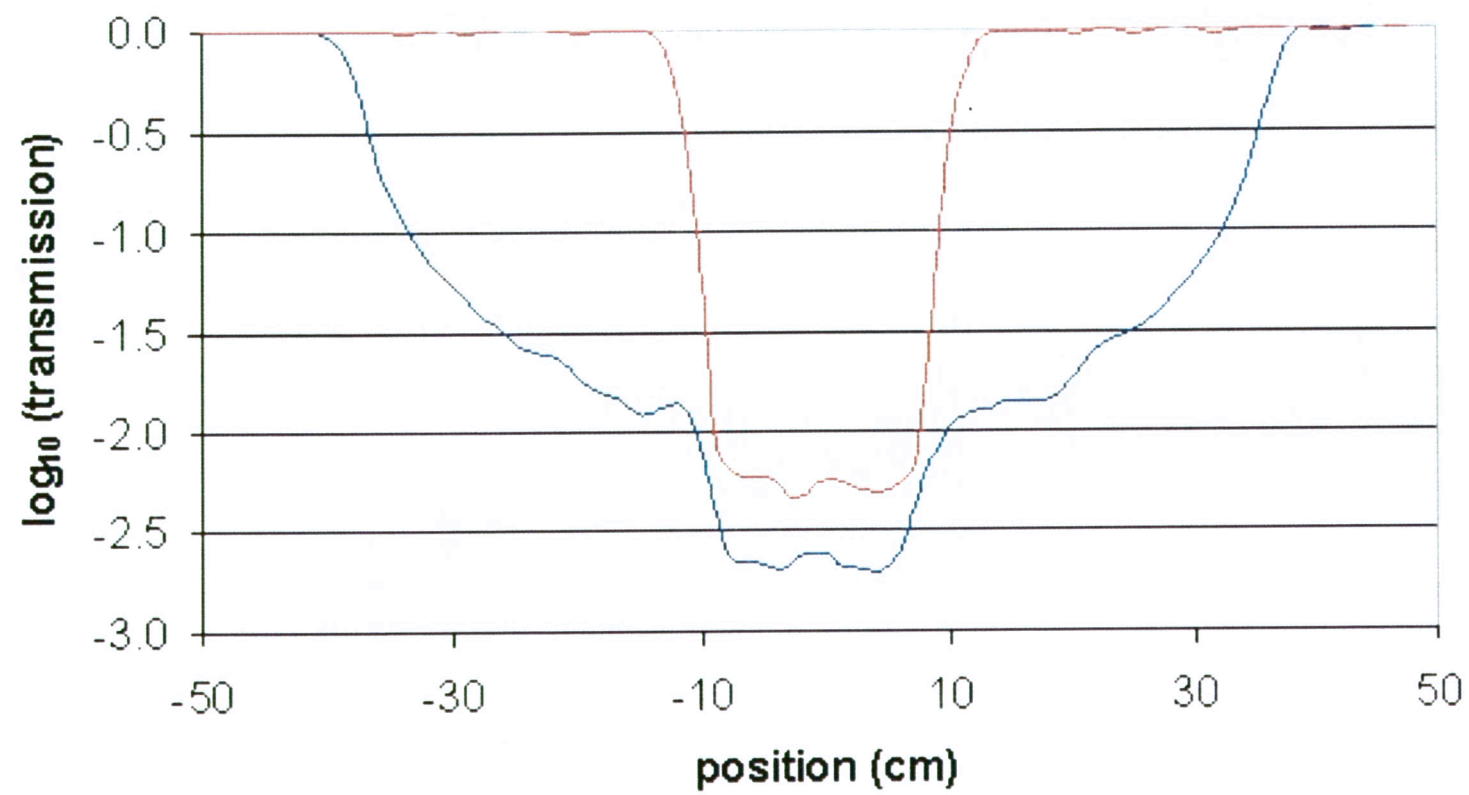


FIGURE 2

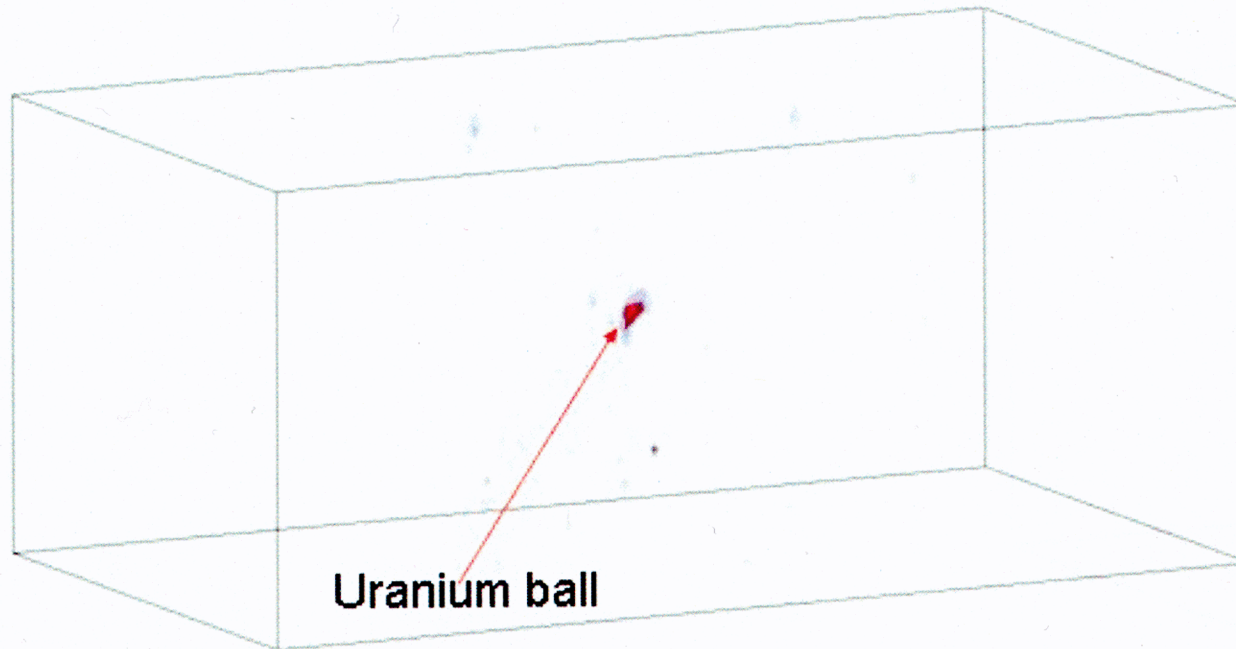


FIGURE 3

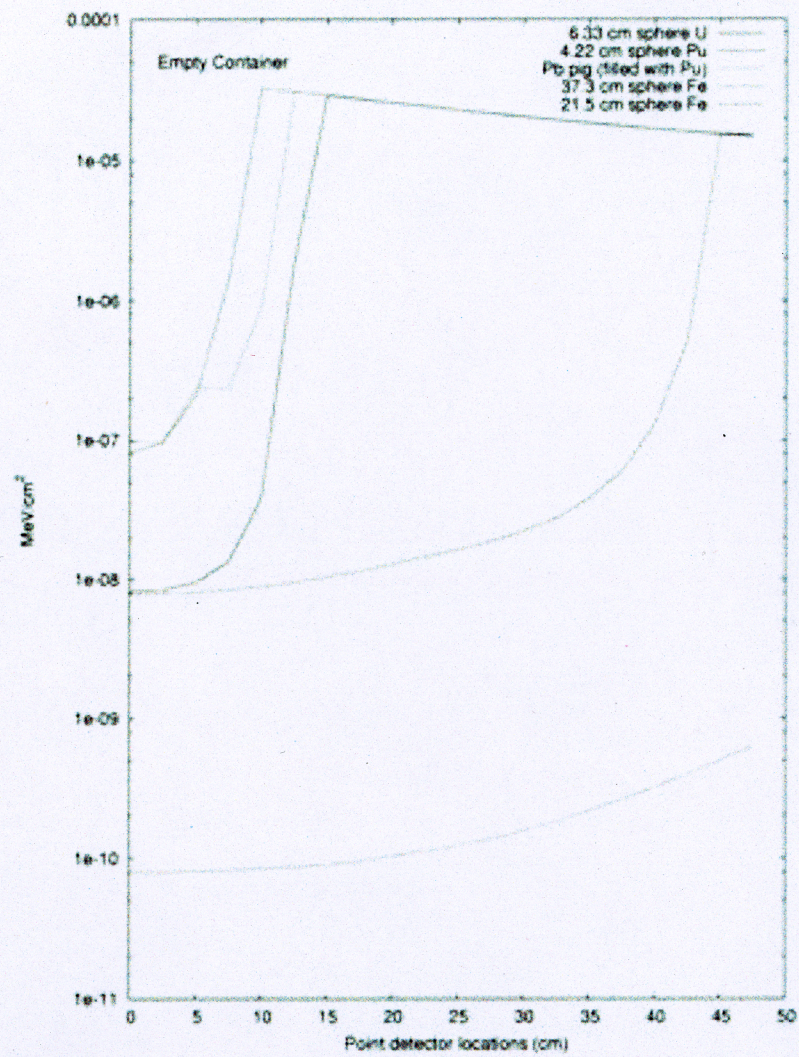


FIGURE 4

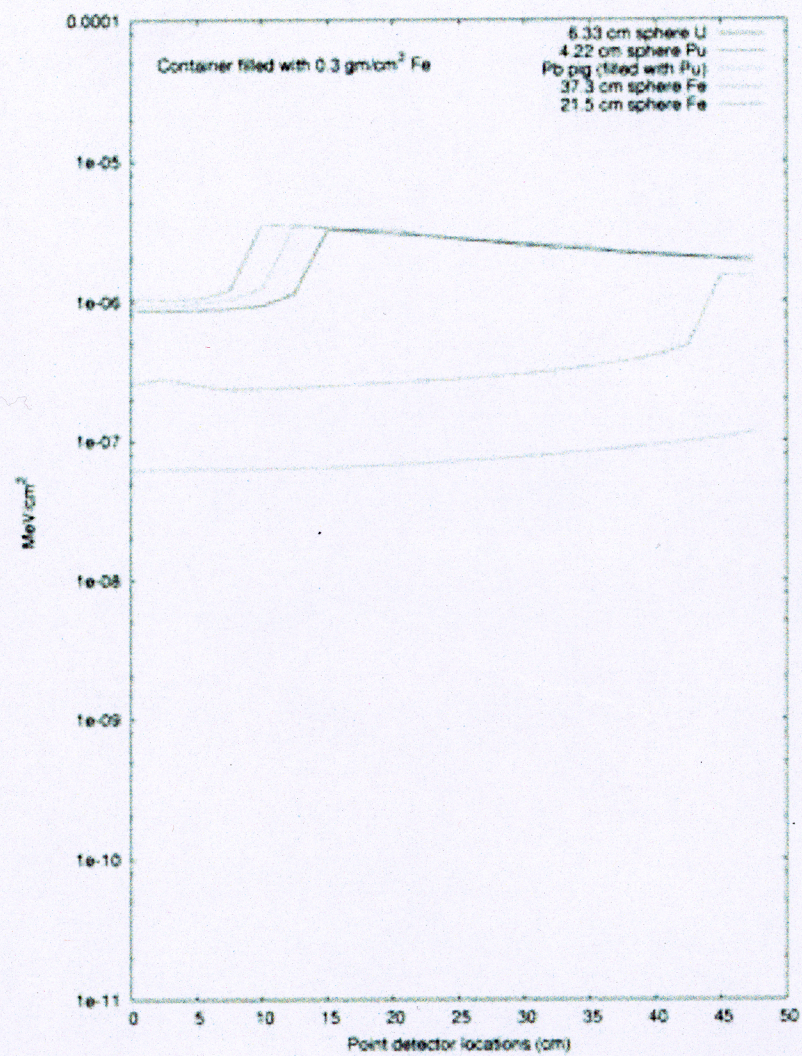


FIGURE 5

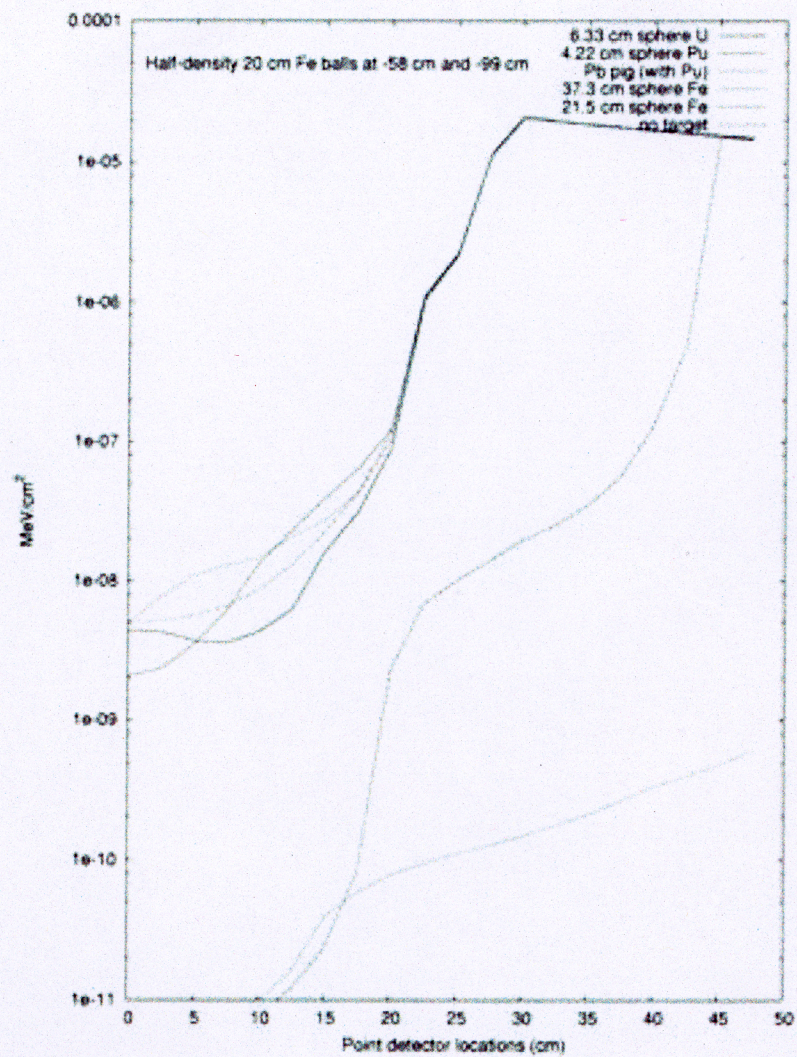


FIGURE 6

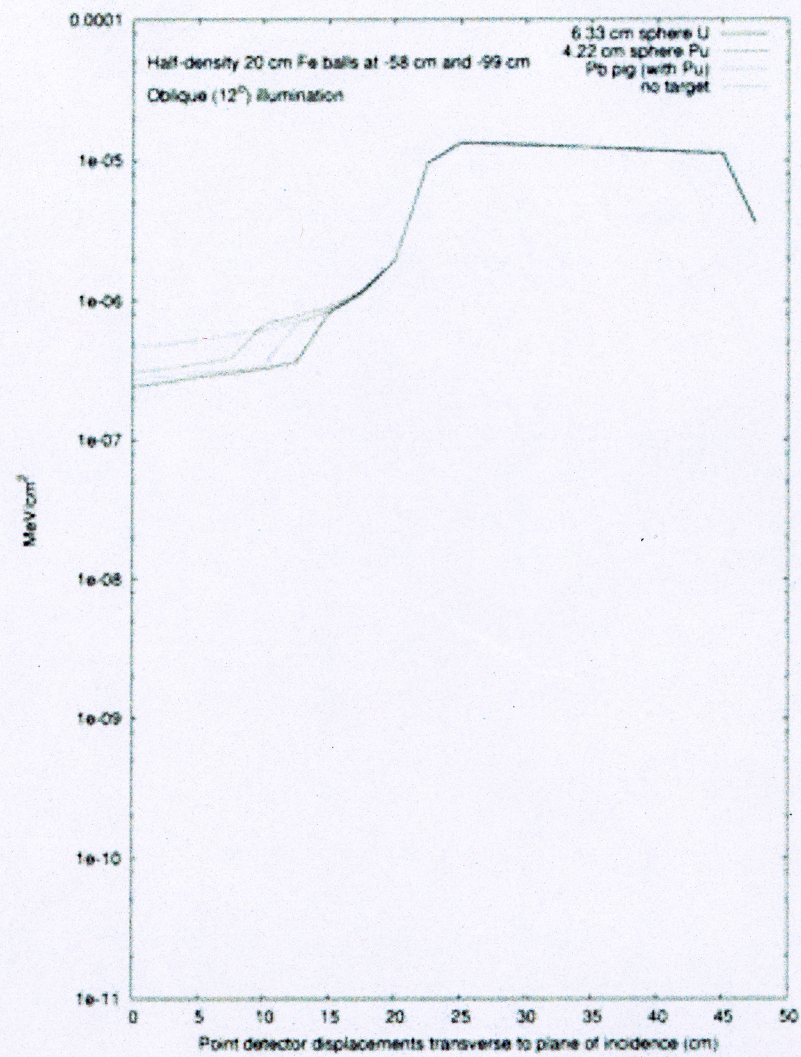


FIGURE 7

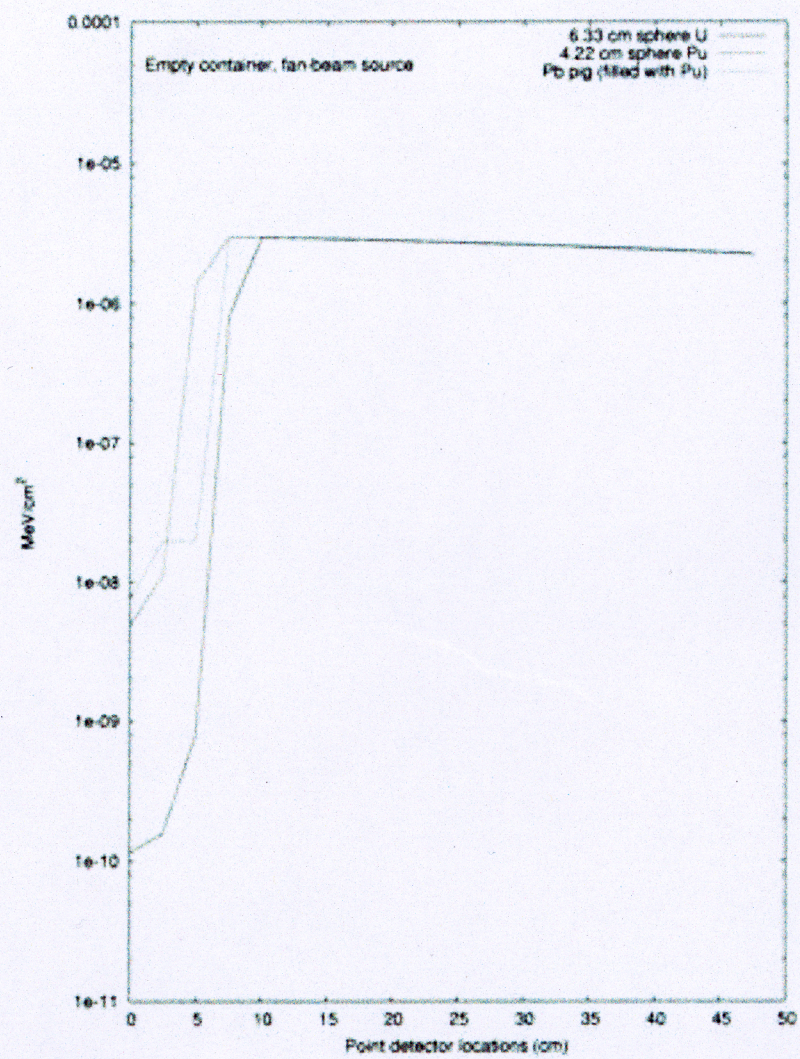


FIGURE 8

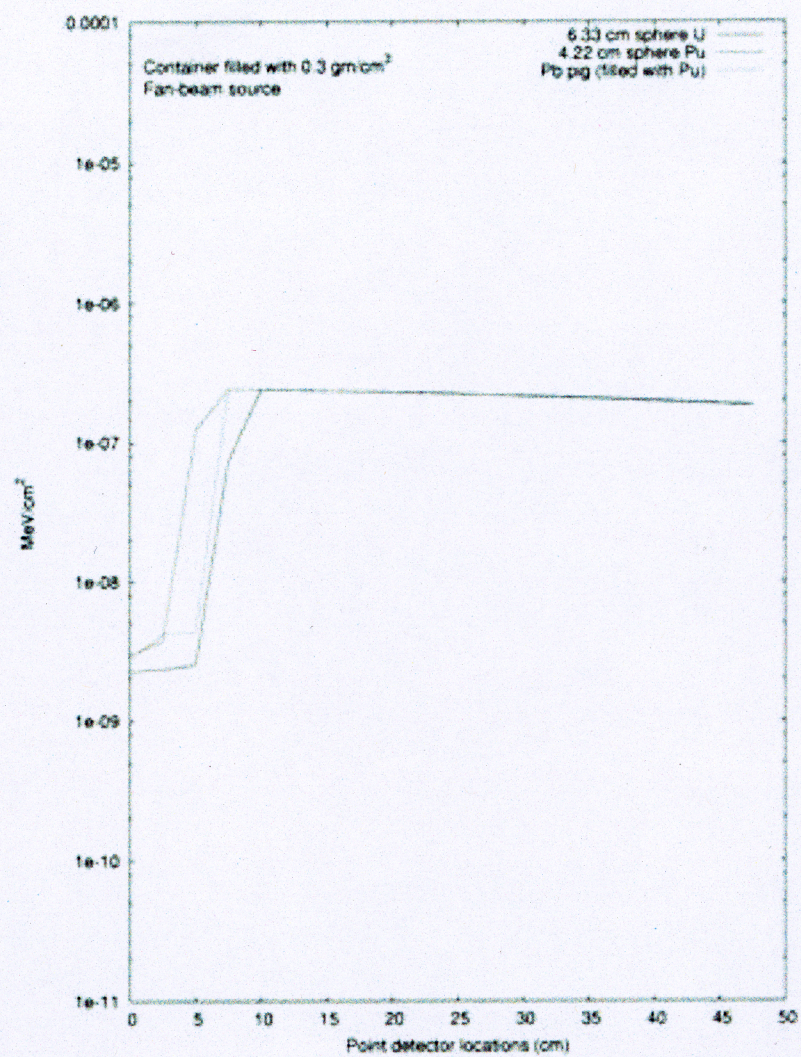


FIGURE 9

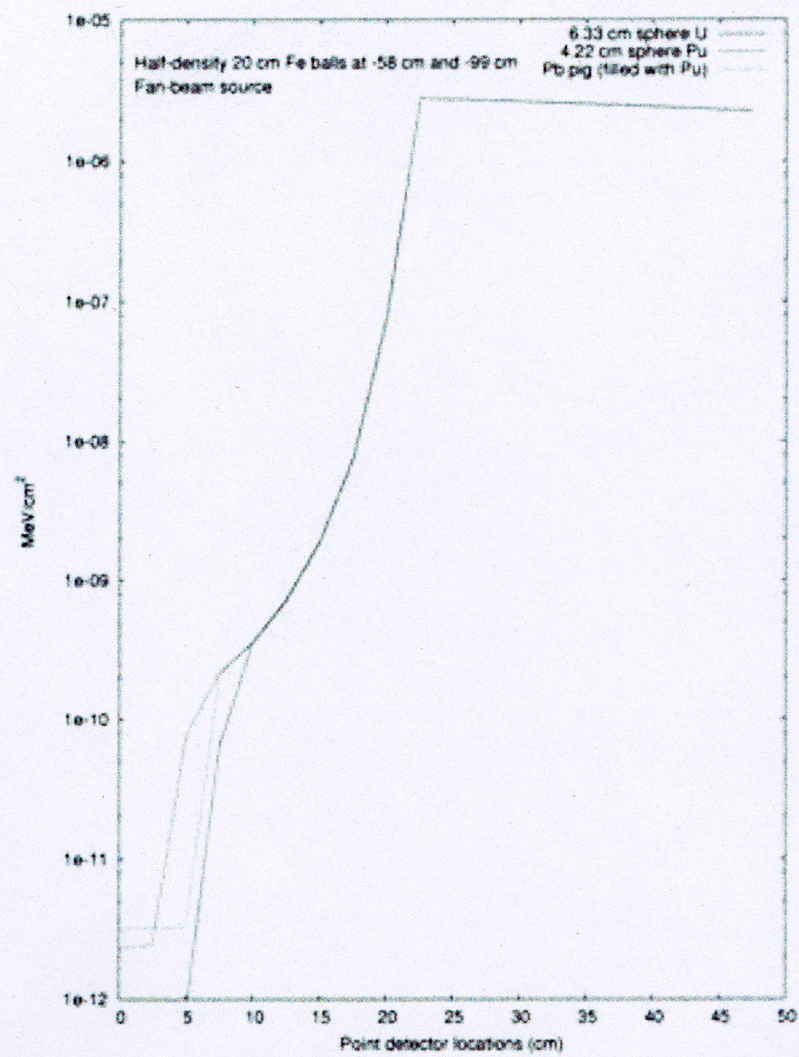


FIGURE 10

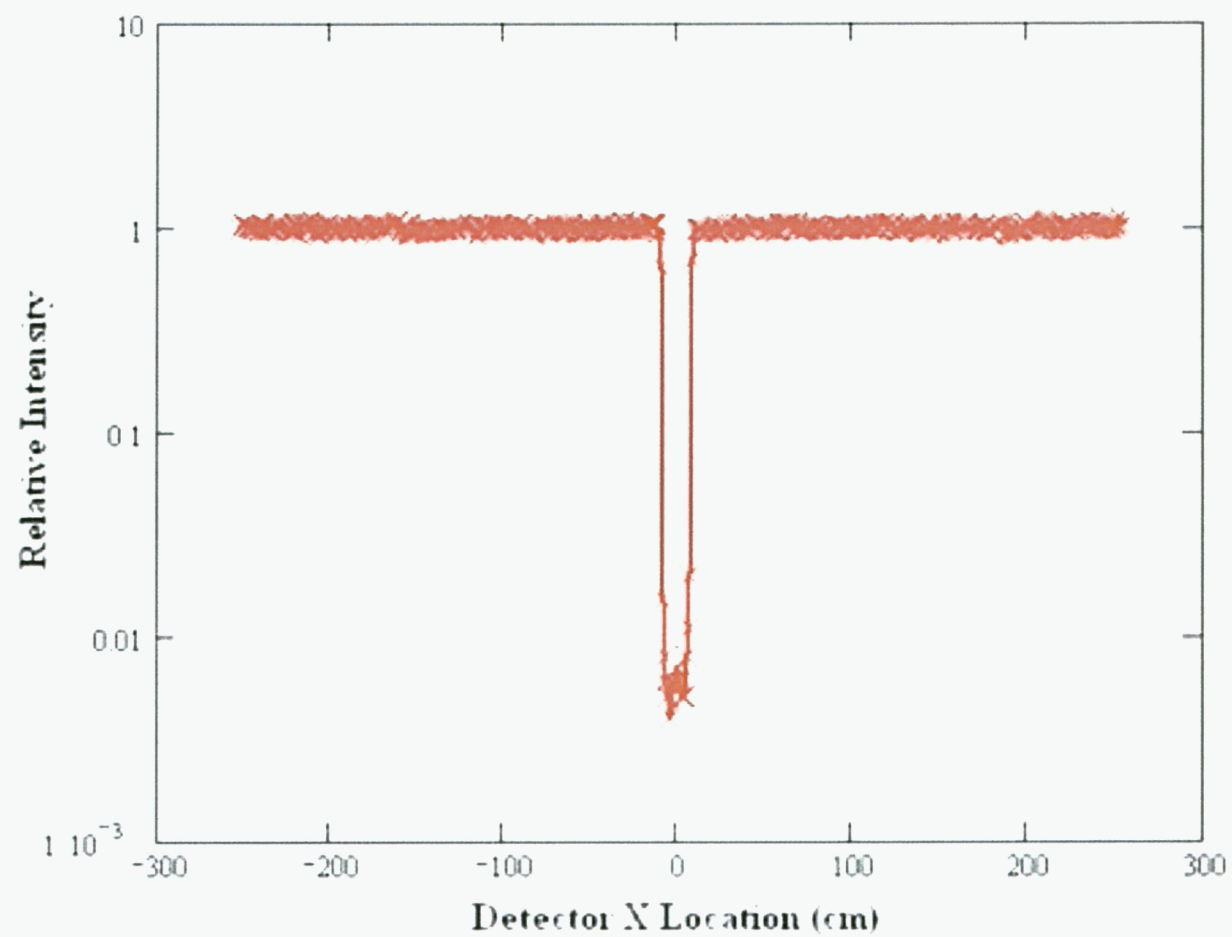


FIGURE 11

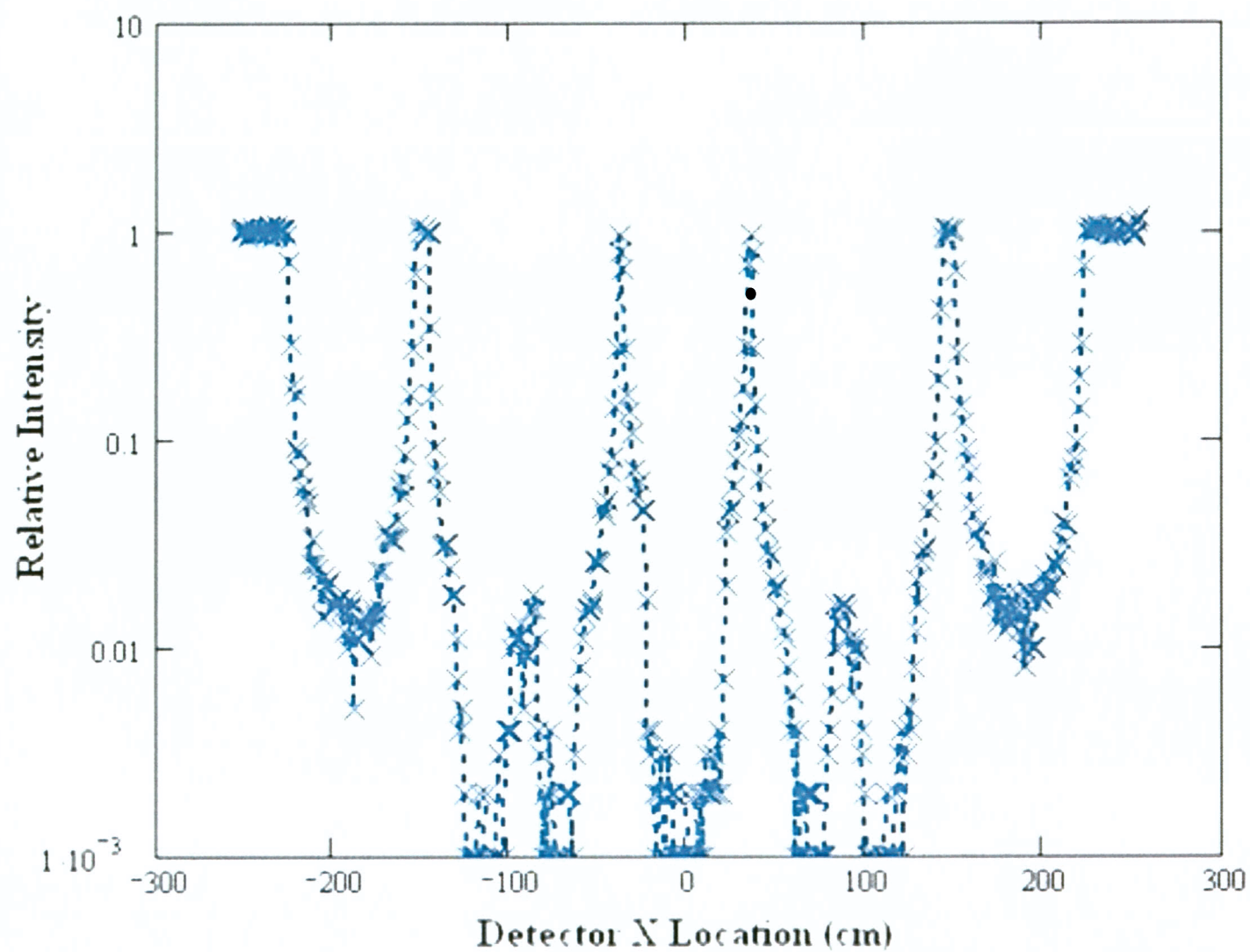


FIGURE 12

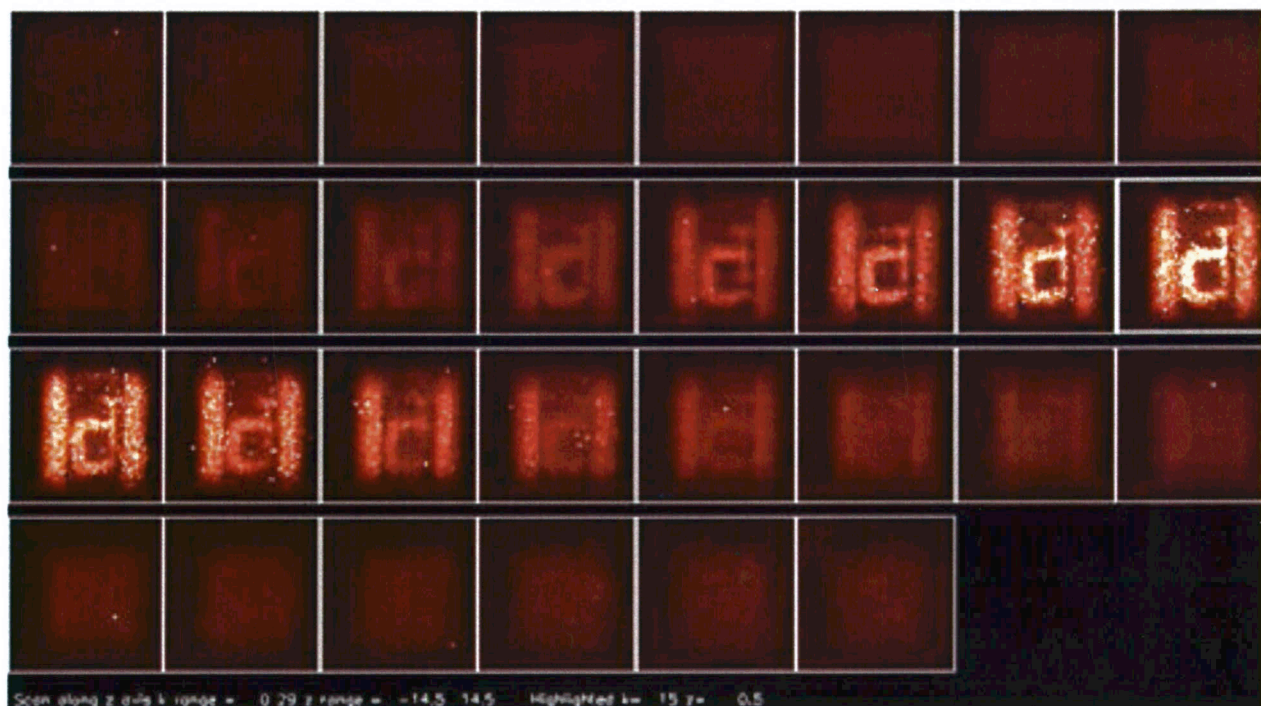


FIGURE 13

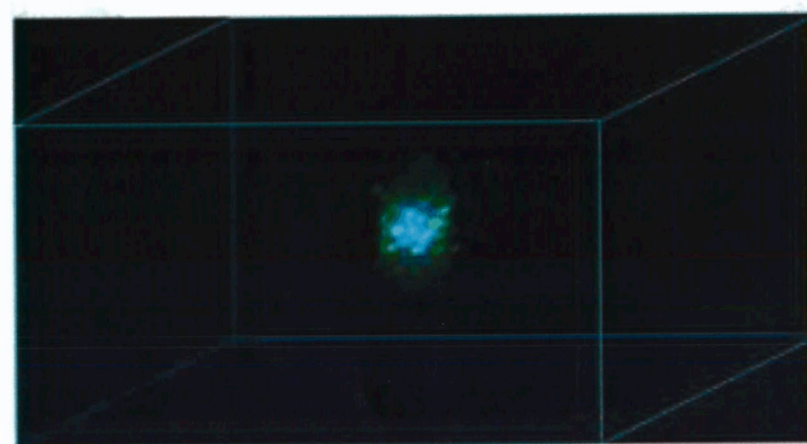
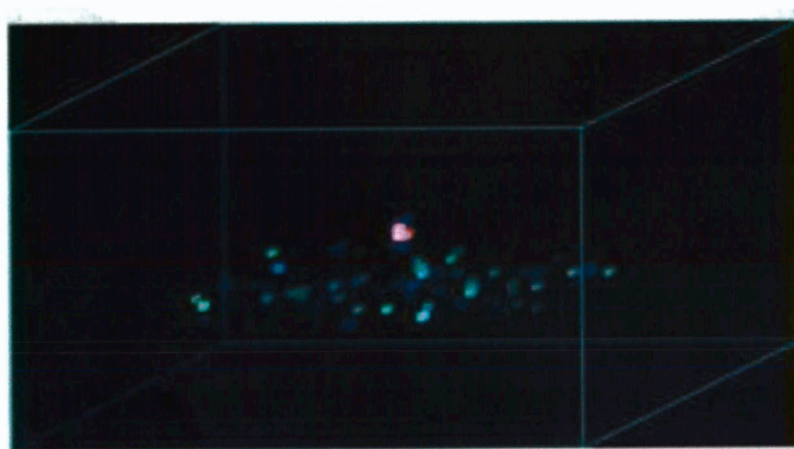
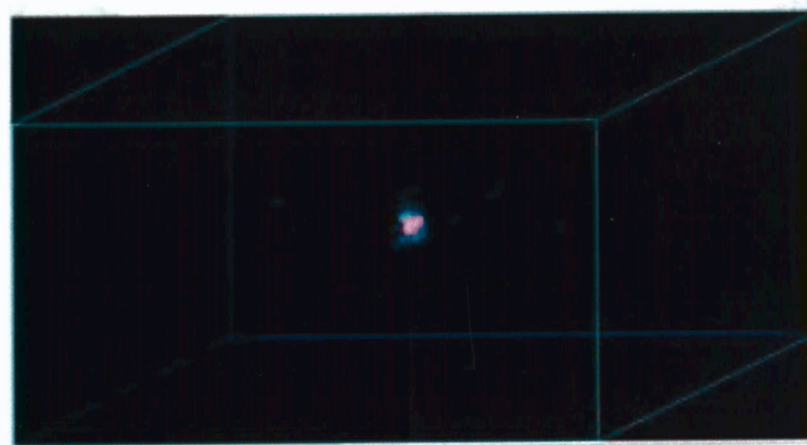
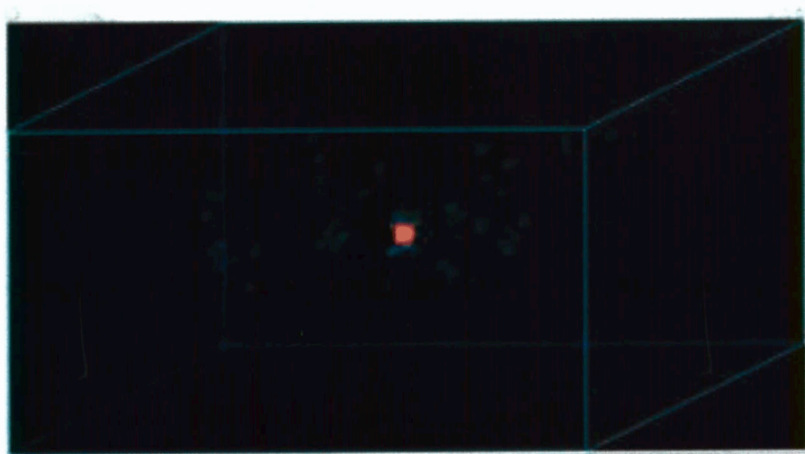


FIGURE 14